International Journal of Steel Structures (2020) 20(4):1378–1392
https://doi.org/10.1007/s13296-020-00369-7

Online ISSN 2093-6311
Print ISSN 1598-2351

A Deformation History-Based Approach for Ultra-Low Cycle Fatigue Damage Evaluation of Steel Structures

Xu Xie[1] · Cheng Cheng[1] · Shuailing Li[1]

Received: 27 November 2019 / Accepted: 4 June 2020 / Published online: 9 June 2020

Abstract

Ultra-low cycle fatigue (ULCF) damage is one of the main failure modes of steel structures when subjected to intense earthquake action, such as near-field action. However, existing ULCF evaluation methods are based on the plastic strain history of structures, which requires fine numerical simulation and causes high calculation cost. In order to improve and simplify the ULCF evaluation process for steel structures, a new damage index based on the structure deformation history was proposed in this paper, with the application of structure life curve and Miner's rule. Two types of steel components, notched round steel bar and steel pier, were employed as the research objectives to verify the accuracy of proposed damage index. The predicted ULCF life was compared with the results of tests and finite element simulations, which showed that the application of damage index was of acceptable accuracy. Compared with the traditional plastic strain history-based ULCF evaluation methods, the advantage of proposed damage index is that ULCF life of a given steel structure can be determined quickly according to the loading condition once its life curve is realized, thus eliminating the cumbersome numerical simulation process.

Keywords Ultra-low cycle fatigue · Damage index · Steel structures · Deformation history · Life curve

Abbreviations

ULCF	Ultra-low cycle fatigue
SHS	Square hollow section
LCF	Low cycle fatigue
CDM	Continuous damage mechanics
CVGM	Cyclic void growth model
FE	Finite element
F	The group code of round bar specimens used to establish the life curve
V	The group code of round bar specimens used to verify the accuracy of proposed index D
PTF	Loading mode: pull to failure
CA	Constant amplitude cyclic loading
C1	One-cycle cyclic loading with a stable increment per cycle
C3	Three-cycle cyclic loading with a stable increment per three cycles
C-PTF	Loading mode: cycle and pull to failure
S4R	4-Node reduced integration shell element
B31	Linear interpolation, three-dimensional beam element
C3D8R	Three dimensional, 8-node reduced integration solid element

Variables

ε_{pD}	The damage strain threshold in pure tension for Tateishi model
$\Delta\varepsilon_p$	Plastic strain range
N_{fL}	LCF initiation life (unit: cycle)
C_p, k_p	Two constants related to Coffin–Manson's relationship
$\Delta\varepsilon$	Strain range
$\Delta\varepsilon_e$	Elastic strain range
l^*	Material characteristic length (unit: m)
$\Delta\delta$	Deformation range of steel structure (unit: mm)
N_f	ULCF life (unit: cycle)
C_δ, k	Two constants related to Eq. (2)
N_{hf}	Half of N_f (unit: half cycle)
k_1, k_2	Two constants related to life curve

✉ Xu Xie
xiexu@zju.edu.cn

Cheng Cheng
11812059@zju.edu.cn

Shuailing Li
11612057@zju.edu.cn

[1] College of Civil Engineering and Architecture, Zhejiang University, Hangzhou 310058, Zhejiang Province, China

D_i	The cumulative damage of structures at *i*th load cycle
$N_{\mathrm{hf},i}$	The ULCF life of steel structure under constant amplitude cyclic loading with the imposed deformation $\Delta\delta$ at *i*th cycle
D	The proposed damage index
$\Delta\delta_i$	The deformation range at the *i*th cycle (unit: mm)
n	The total number of the load cycle (unit: half cycle)
E	Elastic modulus (unit: MPa)
σ_{y}	Yield strength (unit: MPa)
σ_{u}	Ultimate strength (unit: MPa)
A_{l}	Elongation ratio (unit: %)
N_{hc}	The number of half cycles (unit: half cycle)
ε	The strain of extensometer
R^2	Correlation coefficient
N_{hfe}	The ULCF life obtained by tests (unit: half cycle)
N_{hfp}	The ULCF life predicted by proposed method (unit: half cycle)
N_{hfC}	The ULCF life predicted by CVGM (unit: half cycle)
δ_{e}	The fractured deformation obtained by tests (unit: mm)
δ_{p}	The fractured deformation predicted by proposed method (unit: mm)
δ_{C}	The fractured deformation predicted by CVGM (unit: mm)
VGI_{cyclic}	The void growth index
$VGI_{\mathrm{cyclic}}^{\mathrm{critical}}$	The critical void growth index
ε_1	The equivalent plastic strain at the beginning of each tension or compression cycle
ε_2	The equivalent plastic strain at the end of each tension or compression cycle
T	The stress triaxiality
σ_{m}	The hydrostatic pressure (unit: MPa)
σ_{eq}	The Mises stress (unit: MPa)
$\mathrm{d}\varepsilon_{\mathrm{p}}$	The equivalent plastic strain increment
η	The toughness parameter of materials
$\varepsilon_{\mathrm{p}}^{\mathrm{critical}}$	The fracture strain
λ	The degradation parameter of materials
$\varepsilon_{\mathrm{p}}^{\mathrm{accumulated}}$	The cumulative equivalent plastic strain at the beginning of each tension cycle
f	The material damage ratio
λ_{B}	The slenderness ratio
R_{R}	The width-to-thickness ratio
h	The height of piers (unit: mm)
r	The radius of gyration (unit: mm)
B	The width of the compression flange (unit: mm)
t	The thickness of flange and web (unit: mm)
ν	The Poisson's ratio
n_{r}	The number of regions divided by stiffeners in a flange or web
W	The width of the web (unit: mm)
P/P_{y}	The axial compression ratio
a	The spacing of transverse partitions (unit: mm)
γ/γ^*	The relative stiffness of longitudinal stiffeners
t_{s}	The thickness of vertical stiffener (unit: mm)
b_{s}	The width of vertical stiffener (unit: mm)
δ	The imposed deformation (unit: mm)
P	The axial force applied on the top of piers (unit: N)
L_d	The length of effective damage zone (unit: mm)
α	The ratio of a to B
h_{f}	The fillet size (unit: mm)
$\sigma\vert_0$	Initial yield stress
Q_∞	The maximum value of yield surface
b	The change ratio of yield surface with increasing plastic strain
C_1, C_2, C_3	Three initial values of kinematic hardening modulus
γ_1, γ_2, γ_3	Three reduction ratios of kinematic hardening modulus with increasing plastic strain
δ_{y}	The yield displacement (unit: mm)
δ_{y1}	The bending yield displacement (unit: mm)
δ_{y2}	The shear yield displacement (unit: mm)
H_{y}	The yield lateral load (unit: N)
I	The moment of inertia (unit: mm^4)
κ	The shear unevenness coefficient of cross section
G	The shear modulus (unit: MPa)
A_{S}	The sectional area (unit: mm^2)
M_{y}	The yield bending moment (unit: N·mm)
P_{E}	The Euler's buckling axial load (unit: N)
P_{u}	The ultimate axial strength (unit: N)
P_{y}	The yield axial force (unit: N)
δ_{yI}	The yield displacement of steel pier No. S20-30P15
δ_{yII}	The yield displacement of steel pier No. S20-40P15
δ_{yIII}	The yield displacement of steel pier No. S30-30P15
A, C	Two constants in life curve of steel piers

1 Introduction

Ultra-low cycle fatigue (ULCF) damage is the main failure form of steel structures under strong earthquake. During the Northbridge earthquake in 1994 and Kobe earthquake in 1995, ULCF damage was observed primarily at

beam-column joints of steel building structures and base end joints of steel piers (Gates and Morden 1996; Nakashima et al. 1998). The ULCF damage is characterized by the formation of an initial crack at the welded part, which then propagates under cyclic loads, and eventually a brittle-like fatigue fracture occurs. The plastic deformation ability of materials is not fully utilized before the failure of the whole structure. Similar damage modes were also found in several laboratory tests, of which the results showed that the welded part with concentrated strain is the vulnerable site of ULCF failure (Okashiro et al. 2002; Tateishi et al. 2008; Liu et al. 2017; Jia et al. 2015; Ge et al. 2007; Hanji et al. 2011; Ge et al. 2013). For example, in the study of unstiffened cantilever steel columns carried out by Tateishi et al. (2008), all specimens were cracked at corners under cyclic loads followed by stable crack propagation and fractured in the end. The experimental study on a series of welded T-joints under various loading protocols carried out by Liu et al. (2017) showed a ductile-fatigue transition fracture mode, from which fatigue cracks were observed at base metal, weld deposit, heat-affected zone or along fusion line respectively. Jia et al. (2015) investigated the seismic performance of square hollow section (SHS) column, from which two cracking modes, single cracking and multiple cracking, were observed, and strain concentration occurred at the corners similarly. Ge et al. (2007) and Hanji et al. (2011) derived the similar conclusion by the experimental investigation of steel piers and load-carrying cruciform joints respectively. Especially, from the tests of steel piers with thick-walled cross section carried out by Ge et al. (2013), it was found that ductile fracture caused by ULCF is likely to occur before the occurrence of local buckling and generally becomes the governing seismic damage mode.

In order to investigate the mechanism of ULCF damage, Kuwamura (1997) compared the fractured surfaces of materials caused by ULCF and low cycle fatigue (LCF) respectively and discovered that there was a great difference between the two. The former was featured with dimples, indicating that ULCF damage is of ductile cracking and that the Coffin–Manson's relationship determined by LCF tests cannot be directly applied in ULCF field. To improve its accuracy in the field of ULCF, the Coffin–Manson's relationship has been revised and modified by many researchers. For instance, based on the results of material ULCF tests, Tateish et al. (2007) proposed a piecewise formula to predict ULCF life, in which the influence of ductile damage on ULCF life is assumed to be counted once the critical plastic strain ε_{pD} reached; otherwise, this influence can be neglected and the whole model degenerates into the form of the Miner's law. By introducing an exponential function and additional material parameters, Xue (2008) derived a unified expression of fatigue life containing the consideration of both LCF and ULCF domain.

However, the above empirical methods fail to take into account the effect of stress triaxiality. They are thus inapplicable to predict the ULCF life of structures under complex stress state. Attempts were also made by researchers to propose new models to solve this problem according to several micro-mechanism-based theories, such as fracture mechanics, void growth theory and continuous damage mechanics (CDM). Although fracture mechanics has made considerable progress in analyzing structural fatigues, emphasis is placed on the analysis of crack propagation process, which is not suitable for the calculation of steel structures with unobvious initial defects (Zhou et al. 2013). While other two methods do not have such restrictions, thus plastic damage mechanism-based mechanical models have received extensive attention in the analysis of structural ULCF failure. For example, based on the ductile void growth model proposed by Anderson (2005), Kanvinde and Deierlein (2007) developed a semi-empirical and -theoretical approach, i.e., cyclic void growth model (CVGM), to predict the material cracking initiation under cyclic loading. Tong et al. (2016) proposed a CDM-based model to evaluate ULCF damage according to the relationship between triaxial stress and cumulative equivalent plastic fracture strain studied by Bonora (1997). Based on these empirical methods at material level discussed above, other scholars have also carried out researches on ULCF performance at steel structure level. For instance, Ge and Kang (2012) and Kang and Ge (2013) calculated the ULCF life of steel piers under seismic-type cyclic loads, the former adopted Coffin–Manson's relationship, while Teteishi model and Xue model were used by the later; Zhou et al. (2013), Wang et al. (2010) and Xie et al. (2018) applied CVGM to evaluate ULCF performance of steel architectures and steel arch bridges respectively.

However, both empirical methods, such as the Coffin–Manson's relationship and Tateishi model, and semi-empirical approaches, such as CVGM and CDM model, take the local plastic strain history of fatigue crack initiation site as the structural response parameter to estimate the development process of fatigue fracture. Except fine finite element numerical simulation, so far no other effective algorithm can accurately obtain the local plastic strain history. Due to the complexity of calculation process and the large amounts of computation cost, the above approaches are difficult to be applied in practical projects.

To reduce the cost of local strain calculation, simplified methods have been proposed by researchers. For example, Liu et al. (2017) modified the traditional Coffin–Manson's relationship by replacing the plastic strain amplitude with ductility ratio. In terms of its prediction process of crack initiation life, this method eliminates the calculation of plastic strain and appears more convenient for seismic design in practice. Ge and Luo (2011) compared the strain results of fine shell element models with that of fiber analysis and

established an empirical formula of strain concentration coefficient at the bottom of steel bridge piers, from which a practical calculation method of local strain was obtained, without considering the form of weld. By averaging the strains over the effective plane using a weight function in an exponential form, a non-local damage model was proposed by Kang and Ge (2013). The application of this method demonstrated the mesh independent nature, with good accuracy between theory and experiments. Chen and Tateishi (2007) established the correlation between the nominal strain range within effective failure length obtained by beam model analysis and the local strain range at weld toe obtained from fine solid-shell element models, and derived a simplified method of predicting ULCF life only using beam analyses. However, it should be noted that the application of these algorithms is limited, in other word, the simplified form calibrated in these papers may be not reliable for other steel structure forms.

A new method was proposed in this paper to simplify the ULCF evaluation process of steel structures, in which the effects of local strain history and stress triaxility are integrated into macroscopic deformation history of the whole structure and the cumulative process of structure ULCF damage is assessed by Miner's law. Two kinds of steel components, i.e., notched round bars and steel piers, were employed to verify the accuracy of proposed algorithm. A total of 24 experimental tests of notched round bars were performed to analyze the ULCF life; the results were then compared with that predicted by the proposed algorithm. Besides, three different kinds of steel piers were analysis by detailed three-dimensional FE simulation. According to the simulation results, the theoretical ULCF life calculated by CVGM and the predicted ULCF life were also compared. Both experimental investigation and numerical simulation results suggested an applicable accuracy of the proposed method, thereby providing guidance for establishing a practical ULCF evaluation system of steel structures under unidirectional cyclic loads.

2 ULCF Damage Index Based on Deformation History

According to a series of fatigue tests of steel specimens, Coffin and Manson have obtained empirical curves of plastic strain range and fatigue life (Manson 1965; Coffin 1954). Test results showed that there is an obvious linear relationship between the logarithms of the plastic strain range $\Delta\varepsilon_p$ and the logarithms of LCF initiation life N_{fL}, which can be formulated as:

$$\Delta\varepsilon_p \cdot N_{fL}^{k_p} = C_p \tag{1}$$

Equation (1) is known as the Coffin–Manson's relationship, where C_p and k_p are constants, and $\Delta\varepsilon_p = \Delta\varepsilon - \Delta\varepsilon_e$ = plastic strain range, $\Delta\varepsilon$ is strain range, $\Delta\varepsilon_e$ is elastic strain range and it can be calculated by the ratio of peak stress to elastic modulus during loading progress. The relevant parameters in this curve are obtained from the regression of test data. Due to its simplicity, Eq. (1) is widely used for fatigue calculation of steel structures. For example, combining with the beam-to-solid submodeling technique, Basquin law, Manson–Coffin law, and the cumulative damage criteria, Liu et al. (2019) established a global-local fatigue assessment method, by which the fatigue damage can be effectively evaluated for the riveted joints of riveted metallic bridges.

It can be observed from Eq. (1) that the calculation of fatigue life is based on the plastic strain range $\Delta\varepsilon_p$. In order to obtain the plastic strain range of structures subjected to cyclic loads, a fine three-dimensional finite element model is required, of which the mesh size should represent the material characteristic length l^* (Kanvinde 2004). This method is computationally intensive, and the result of $\Delta\varepsilon_p$ has a strong dependence on element type and mesh size. What's more, the Coffin–Manson's relationship is founded according to large amounts of uniaxial tension tests, the effect of stress triaxility is not taken into account. Thus, its application under complex stress state is not available.

The problem discussed above is improved in this paper. Attempts were made to replace $\Delta\varepsilon_p$ with the macroscopic deformation response $\Delta\delta$ in the cyclic loading process, by which the effects of the whole system mechanics, such as material ductility, structural parameters and triaxial stress, are considered. Then, the Coffin–Manson's relationship is updated to the following form:

$$\Delta\delta \cdot N_f^k = C_\delta \tag{2}$$

where N_f is structure ULCF life; C_δ and k are constants; $\Delta\delta$ is the deformation range, reflecting the loading history of structures, it can be expressed as the imposed axial deformation applied at both ends for notched round bars and horizontal deformation range at the top of piers for single column steel piers.

By replacing the ULCF life N_f with N_{hf} (unit: half cycle, $N_{hf} = 2N_f$), Eq. (2) can be rewritten as the following form:

$$N_{hf} = 2k_1 \cdot \Delta\delta^{k_2} \tag{3}$$

where k_1 and k_2 are the two constants of the life curve, $k_1 = C_\delta^{1/k}$, $k_2 = -1/k$, and these two constants are obtained by the regression fitting of data ($\Delta\delta$, N_{hf}) derived from constant amplitude loading tests. In this paper, Eq. (3) is called life curve of steel structures.

According to the Miner's law, the cumulative damage of structures at each load cycle can be defined as $D_i = 1/$

$N_{hf,i}$, in which $N_{hf,i}$ refers to the ULCF life of steel structure under constant amplitude cyclic loading with the imposed deformation at ith cycle. For the structures under variable deformation amplitude, the cumulative damage index D can be written as follows:

$$D = \sum_{i=1}^{n} \frac{1}{N_{hf,i}} = \frac{1}{2k_1} \sum_{i=1}^{n} \left(\Delta\delta_i\right)^{-k_2} \tag{4}$$

where $\Delta\delta_i$ refers to the deformation range at the ith cycle and $N_{hf,i}$ means the ULCF life corresponding to the constant amplitude loads of deformation range $\Delta\delta_i$, n denotes the total number of the load cycle. The cumulative damage index D is equal to zero when there is no damage and it is assumed that structural failure would occur if $D = 1$ is satisfied.

When calculating ULCF damage of structures according to Eq. (4), there is no need to obtain plastic strain range $\Delta\varepsilon_p$ under cyclic loading, and the ULCF life can be quickly derived only by the structure deformation history.

3 Validation Tests of Round Bar Specimens

In order to verify the accuracy of the damage index D featured with deformation response parameter in evaluating ULCF performance of steel structures, notched round bars and steel bridge piers were employed in this paper. The validity verification of notched round bar specimens is described in this section first and steel piers numerical simulation can be found in Sect. 4.

3.1 Specimen and Test Device

The configuration and dimension of round bar specimens used for validation tests are shown in Fig. 1. In order to ensure the occurrence of ULCF damage, the notch radius of selected samples is designed as 1.80 mm. Specimens were made of Q345qC steel, which is commonly used in Chinese steel bridges. The mechanical properties are shown in Table 1.

Uniaxial tensile tests of circular notched specimens were carried out using MTS 880 (MTS Systems Corporation, Eden Prairie, MN, USA), which is shown in Fig. 2. The uniaxial deformation process of specimens was controlled by the loading strain of extensometer, of which the gauge length is 50 mm.

3.2 Sample Grouping and Loading Procedure

Notched round bar specimens were divided into two groups: F and V. Group F was used to establish the fatigue life curve, and group V was used to verify the accuracy of proposed damage index D. The loading patterns of group F are PTF (pull to failure) loading and CA (constant amplitude) cyclic loading. Under PTF loading, the specimen's ULCF life is assumed as 1.0 (unit: half cycle); while under CA loading, the specimen is cycled within designed deformation limits until ULCF crack occurs.

In group V, the loading patterns include C1, C3, CA, Random and C-PTF loadings. Under C1 loading, the imposed deformation increases with each cycle, and the increment remains to the initial amplitude. The loading pattern of C3 is the same as C1 loading, except that the loop period is three instead of one. As an irregular loading mode, Random loading consists of several half-cycles with different imposed deformation amplitudes. C-PTF loading refers to

Table 1 Mechanical properties of Q345qC steel (Li et al. 2019)

E (MPa)	σ_y (MPa)	σ_u (MPa)	A_l (%)
198,221	351.10	508.57	40.60

E indicates elastic modulus; σ_y and σ_u denote the yield strength and ultimate strength respectively; A_l represents elongation ratio

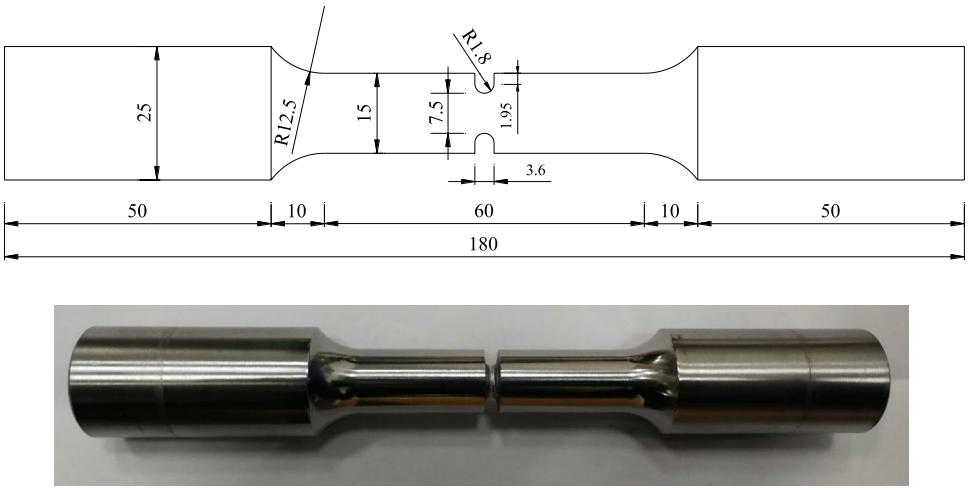

Fig. 1 The steel notched round bar specimen (unit: mm)

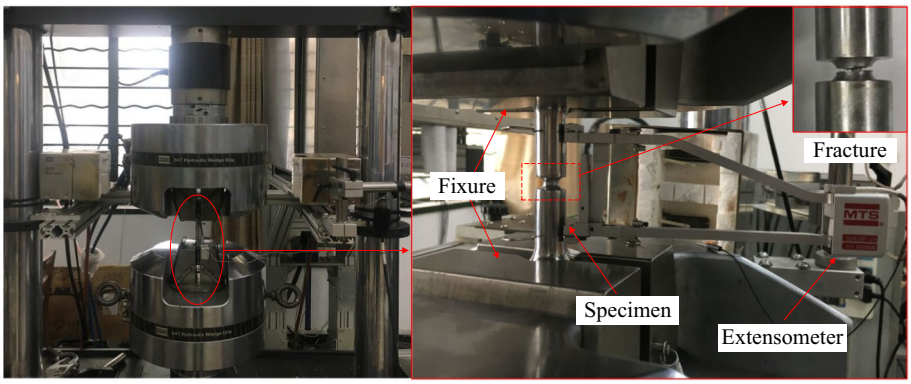

Fig. 2 Setup of notched round bar experiments

cycle and pull to failure, under which the specimen is cycled with constant amplitude deformation for several cycles and then pull to fracture. These six loading patterns explained above are shown in Fig. 3, in which the abscissa indicates the number of half cycles N_{hc}, and the ordinate indicates the strain of extensometer ε. To avoid the buckling instability of samples during compression, all loading modes were designed to make the specimens in tension side as depicted in Fig. 3. Besides, according to the Specification (2008), the strain rate was selected as a constant, of which the value is 0.05%/s. Given the dispersion of steel material itself and the error of sample manufacture, two samples were set for each pattern to ensure the accuracy of tests. Tables 2 and 3 display the data of samples in groups F and V, respectively. In these two tables, CA loading is defined by the number described in the parentheses, which means the loading strain range. And the deformation range of each CA loading can be derived by multiplying its loading strain amplitude by the gauge length 50 mm. For instance, the loading condition CA-(0 → 1.30%) for specimen ETS-9 refers that specimens are subjected to CA loading between loading displacement 0 and 0.65 mm, corresponding to the strain range of 0 and 1.30%. Also, C-PTF loading is featured by two numbers listed in parentheses, denoting the cycles and corresponding strain amplitude respectively. For example, the loading condition C-PTF (5–1%) for VTS-9 and VTS-10 refers that specimens are subjected to five complete cycles between deformation 0 and 0.5 mm, followed by pulling to fracture. Further, the $\Delta\delta$ for PTF loading listed in Table 2 and the δ_e for C-PTF loading listed in Table 3 represent the elongation distance of extensometer section at the end of each loading respectively.

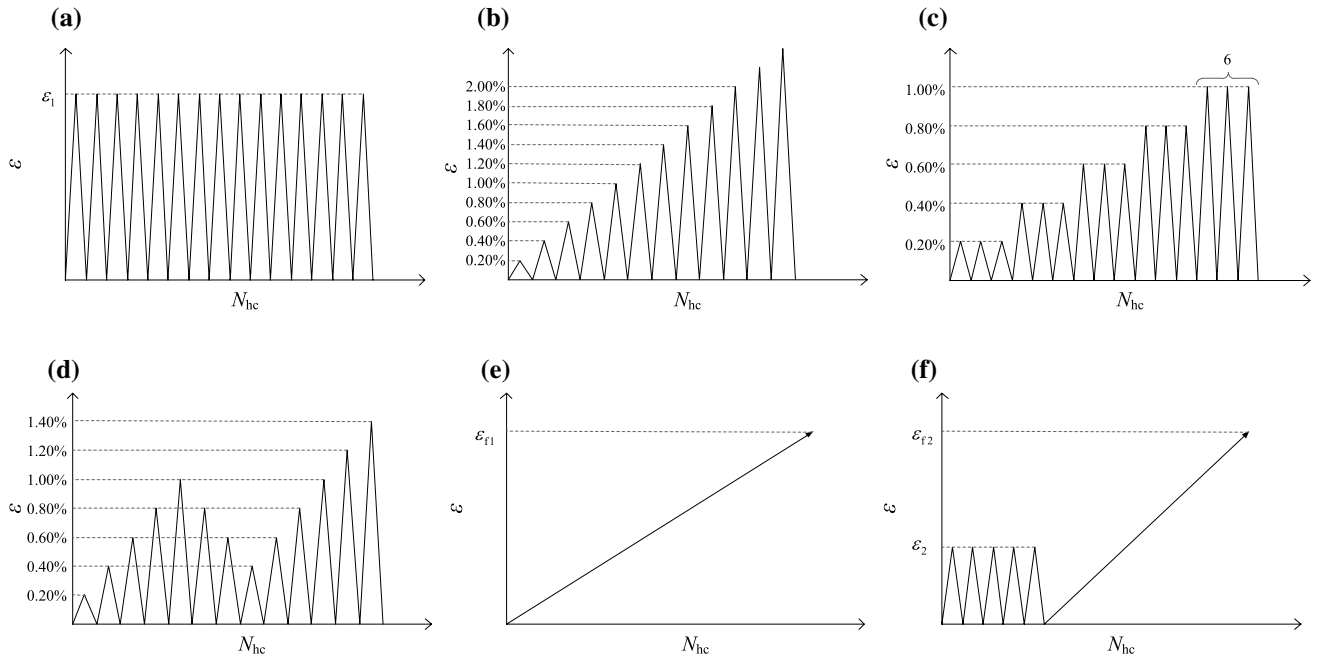

Fig. 3 Loading patterns for round bar specimens **a** CA loading, **b** C1 loading, **c** C3 loading, **d** random loading, **e** PTF loading and **f** C-PTF loading

Table 2 Experimental results of group F

No.	Loading pattern	$\Delta\delta$ (mm)	N_{hf} (half cycle)
ETS-1	PTF	1.170	1.00
ETS-2		1.210	
ETS-3	CA-(0→1.00%)	0.500	34.74
ETS-4			30.80
ETS-5	CA-(0→1.15%)	0.575	20.86
ETS-6			20.70
ETS-7	CA-(0→1.25%)	0.625	18.70
ETS-8			14.86
ETS-9	CA-(0→1.30%)	0.650	12.56
ETS-10	CA-(0→1.35%)	0.675	10.60
ETS-11	CA-(0→1.50%)	0.750	6.70
ETS-12			6.78
ETS-13	CA-(0→1.80%)	0.900	4.96
ETS-14			4.88

Table 3 Experimental results of group V

No.	Loading pattern	N_{hfe} (half cycle)	δ_e (mm)
VTS-1	C1	16.70	–
VTS-2		14.96	–
VTS-3	C3	34.72	–
VTS-4		36.80	–
VTS-5	CA (0→1.40%)	10.76	–
VTS-6		8.76	–
VTS-7	Random	28.42	–
VTS-8		26.64	–
VTS-9	C-PTF (5–1%)	–	1.045
VTS-10		–	1.055

Taking C3 loading as an example, Fig. 4 shows two complete load-deformation curves, in which the abscissa represents the axial deformation of round bar specimens, and the ordinate denotes the applied axial load.

3.3 Life Curve and Verification

According to the 14 sets of data ($\Delta\delta$, N_{hf}) obtained from test results of group F, the life curve function of notched round bar samples can be fitted into Eq. (3) to obtain:

$$N_{hf} = 2.3807 \cdot \Delta\delta^{-3.923} \tag{5}$$

The ULCF life curve corresponding to the Eq. (5) is shown in Fig. 5, from which it is observed that these data points can be approximately fitted by the power function relationship and its correlation coefficient R^2 reaches a high value of 0.9776.

According to Eq. (5), damage index D of notched round bar specimens tested in this paper can be formulated from Eq. (4) as:

$$D=\frac{1}{k_1}\sum_{i=1}^{n}\left(\Delta\delta_i\right)^{-k_2}=\frac{1}{2.3807}\sum_{i=1}^{n}\left(\Delta\delta_i\right)^{3.923} \tag{6}$$

In order to verify the accuracy of proposed damage index D, efforts were made to compare the predicted ULCF life obtained from Eq. (6) with test results of group V. Specimens under C1 loading are taken as examples to illustrate the prediction process herein. For specimens VTS-1 and VTS-2, the loading strain during the first loop is 0.2% and thus the corresponding deformation is 0.1 mm. Combining these data and Eq. (6), the ULCF damage value of the first loop can be calculated and the cumulative damage after the end of each loop can be obtained by analogy. It can be found that when $n=18$, the cumulative damage $D=1.3138$, exceeding 1.0;

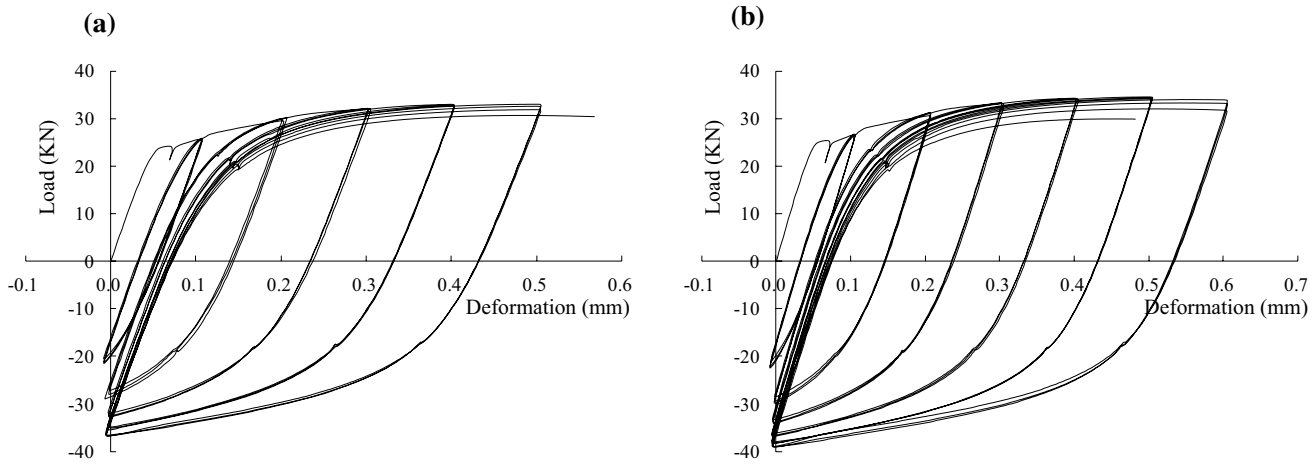

Fig. 4 Load-deformation curves **a** VST-3, **b** VST-4

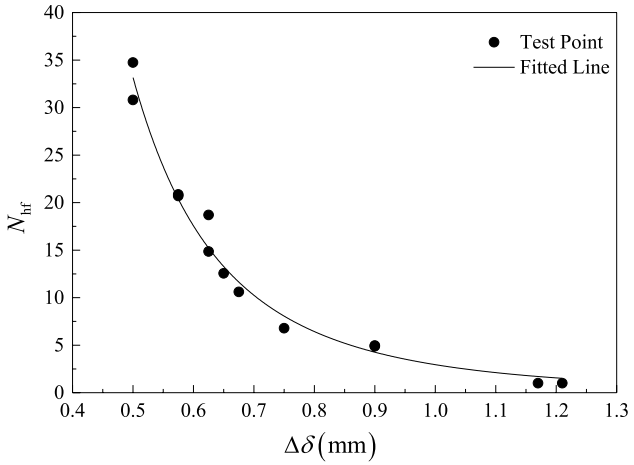

Fig. 5 Life curve of notched round bar specimens

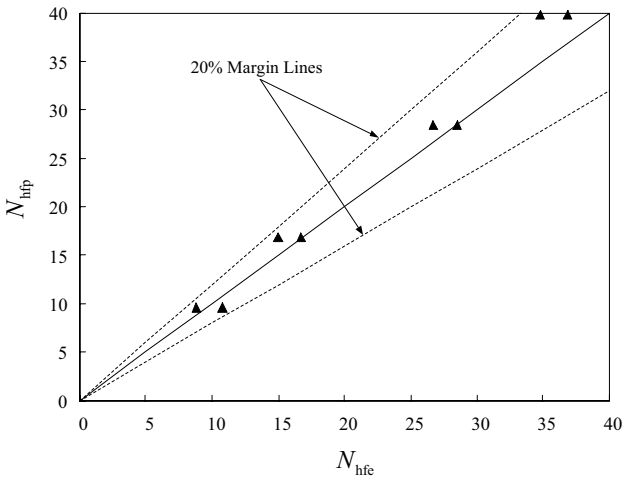

Fig. 6 Comparison between predicted life and experimental life of notched round bar specimens

and the cumulative damage value is 0.7581 when $n=16$, less than 1.0. According to linear interpolation it is not difficult to determine the predicted lifetime as 16.87. By this way, the ULCF life of all specimens of group V can be predicted by index D, which are shown in Table 4. Herein, N_{hfp} means the ULCF life predicted by Eq. (6); N_{hfC} and δ_C are the ULCF life and fractured deformation predicted by CVGM respectively, they will be introduced in Sect. 4.3.

Figure 6 shows that the ULCF damage of all specimens under cyclic loading occurs within 20 cycles (40 half-cycles). The error between the fatigue life predicted by Eq. (6) and the experimental life is controlled within 20%, which suggests a good consistency.

4 Feasibility Verification of Steel Piers

In addition to the notched round bar specimens introduced in Sect. 3, the verification of single-column steel piers was also carried out in this section. Since the full-scale test of steel piers requires great cost of material and time, it is unpractical to obtain the corresponding ULCF mechanical performance from a series of model tests. Given that CVGM could take into account the effects of triaxial stress and roughly reflect the ULCF damage characteristics of steel piers (Zhou et al. 2013; Wang et al. 2010; Xie et al. 2018), the theoretical results of CVGM instead of full-scale tests were used.

4.1 CVGM and Calibrated Parameters

Kanvinde and Deierlein (2007) proposed cyclic void growth model (CVGM) for predicting ULCF life of materials, consisting of a cyclic void growth index VGI_{cyclic} and a cyclic void growth "capacity" $VGI_{cyclic}^{critical}$, which can be expressed as the following forms:

Table 4 ULCF life comparison of group V

No.	ULCF life (half cycle)			Fracture deformation (mm)		
	N_{hfe}	N_{hfp}	N_{hfC}	δ_e	δ_p	δ_C
VTS-1	16.70	16.87	16.70	–	–	–
VTS-2	14.96			–		
VTS-3	34.72	39.84	36.80	–	–	–
VTS-4	36.80			–		
VTS-5	10.76	9.65	8.98	–	–	–
VTS-6	8.76			–		
VTS-7	28.42	28.45	26.76	–	–	–
VTS-8	26.64			–		
VTS-9	–	–	–	1.045	1.148	0.948
VTS-10	–			1.055		

$$VGI_{\text{cyclic}} = \sum_{\text{tensile}} \int_{\varepsilon_1}^{\varepsilon_2} \exp(|1.5T|)\mathrm{d}\varepsilon_{\text{p}} - \sum_{\text{compressive}} \int_{\varepsilon_1}^{\varepsilon_2} \exp(|1.5T|)\mathrm{d}\varepsilon_{\text{p}} \tag{7}$$

$$VGI_{\text{cyclic}}^{\text{critical}} = \eta \cdot \exp\left(-\lambda \varepsilon_{\text{p}}^{\text{accumulated}}\right) \tag{8}$$

where ε_1 and ε_2 represent the equivalent plastic strain at the beginning and end of each tension or compression cycle respectively; $T = \sigma_{\text{m}}/\sigma_{\text{eq}}$ is the dimensionless stress triaxiality, σ_{m} denotes hydrostatic pressure and σ_{eq} indicates Mises stress; $\mathrm{d}\varepsilon_{\text{p}} = \sqrt{(2/3)d\varepsilon_{ij}^{\text{p}} d\varepsilon_{ij}^{\text{p}}}$ is the equivalent plastic strain increment; η means the toughness parameter of materials during monotonic loading, and its corresponding calculation formula is $\eta = \int_0^{\varepsilon_{\text{p}}^{\text{critical}}} \exp(1.5T)d\varepsilon_{\text{p}}$, where $\varepsilon_{\text{p}}^{\text{critical}}$ means the fracture strain under this loading mode; λ represents the degradation parameter of materials under cyclic loading and $\varepsilon_{\text{p}}^{\text{accumulated}}$ is the cumulative equivalent plastic strain at the beginning of each tension cycle. Define f as material damage ratio:

$$f = VGI_{\text{cyclic}}^{\text{critical}}/\eta = \exp\left(-\lambda \varepsilon_{\text{p}}^{\text{accumulated}}\right) \tag{9}$$

It is assumed that ULCF cracking occurs when VGI_{cyclic} exceeds $VGI_{\text{cyclic}}^{\text{critical}}$.

When using CVGM for structure ULCF life prediction, the calibration of toughness parameter η and damage degradation parameter λ is required. According to our previous study, parameter η of Q345qC steel is determined as 2.03 and λ is related to the magnitude of triaxial stress (Li et al. 2019). In this paper, previous test results and several experimental tests supplemented were used to determine the degradation parameter λ, among which the triaxial stress at vulnerable site is controlled within a specific range. The supplementary tests still applied round bar specimens shown in Fig. 1, the only difference was that the notch radii were selected as 1.80, 3.75 and 6.00 (in mm) herein. Table 5 exhibits the corresponding loading modes of supplementary tests. And according to the condition that test results are consistent with FEM analysis results (Kanvinde and Deierlein 2007), the degradation parameter λ can be fitted by data group $\left(\varepsilon_{\text{p}}^{\text{accumulated}}, f\right)$ and Eq. (9). Figure 7 shows the calibrated results of the parameter λ, in which the previous data were taken from literature (Li et al. 2019). Under the considered range of triaxial stresses, the result is obtained as $\lambda = 0.10$.

4.2 Structure Parameters of Steel Piers

Stiffened single-column steel piers with rectangular section are analyzed in this paper, of which the configurations and section details are shown in Fig. 8. All samples were made of Q345qC steel. Local buckling and ULCF failure are the main damage forms of steel piers under strong earthquake, and the corresponding structural parameters are slenderness ratio λ_{B} and width-to-thickness ratio R_{R}, which can be expressed as follows:

$$\lambda_{\text{B}} = \frac{2h}{r}\frac{1}{\pi}\sqrt{\frac{\sigma_{\text{y}}}{E}} \tag{10}$$

$$R_{\text{R}} = \frac{B}{t}\sqrt{\frac{12(1-\nu^2)}{4\pi^2 n_{\text{r}}^2}}\sqrt{\frac{\sigma_{\text{y}}}{E}} \tag{11}$$

where h is the height of piers, r is the radius of gyration; B is the width of the compression flange; t is the thickness of flange and web; ν is Poisson's ratio; and n_{r} is the number of regions divided by stiffeners in a flange or web.

Table 5 Summary of supplemented tests for the calibration of λ

Notch size (mm)	Loading modes	No.	$\varepsilon_{\text{p}}^{\text{accumulated}}$	f
$R = 1.80$ mm	C-PTF 5(0-0.5%)	BMC-1	0.252	0.878
		BMC-2	0.252	0.919
	C-PTF 5(0-1.0%)	BMC-3	0.918	0.930
		BMC-4	0.918	0.930
$R = 3.75$ mm	CA (0-1.0%)	BMC-5	8.320	0.415
		BMC-6	8.047	0.431
	CA (0-1.5%)	BMC-7	2.550	0.608
		BMC-8	2.960	0.575
$R = 6.00$ mm	CA (0-1.5%)	BMC-9	4.850	0.591
		BMC-10	4.850	0.616
	CA (0-2.0%)	BMC-11	2.913	0.680
		BMC-12	2.913	0.834

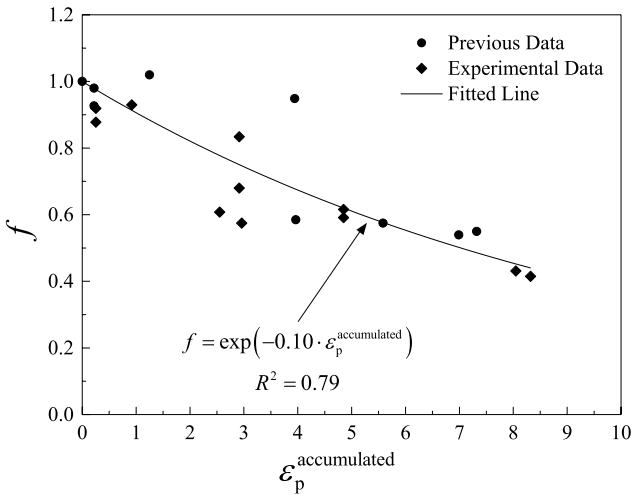

Fig. 7 Scatter plot and fitted curve of damage degradation parameter for Q345qC

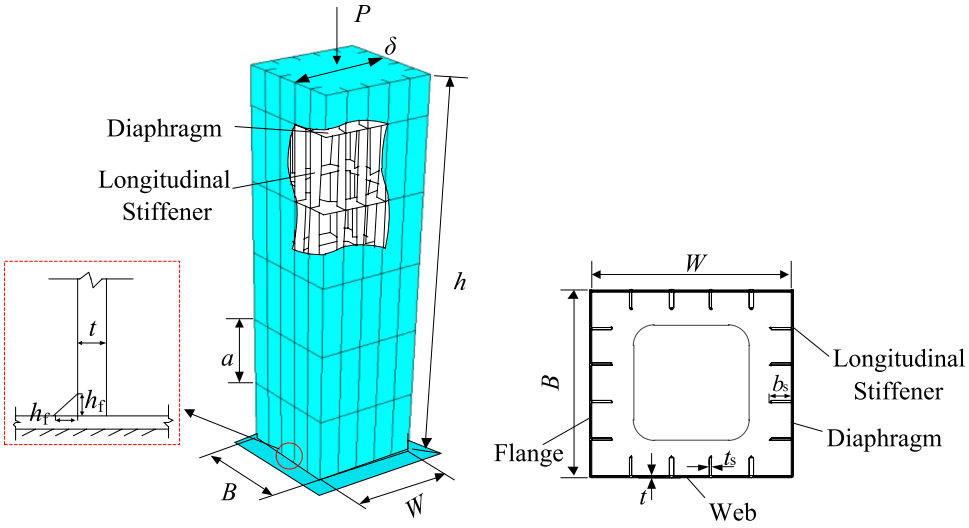

Fig. 8 Schematic diagram of steel piers

The failure modes of steel pier members under cyclic loads studied by Ge et al. (2013) suggested that steel bridge piers are more prone to local instability failure as the width-thickness ratio increases and a larger slenderness ratio could also lead to local instability. Therefore, to guarantee that ULCF failure occurs preferentially for designed steel piers, the selected slenderness ratio and width-thickness ratio should not be too large. In order to compare the influence of different structural parameters on the evaluation results of ULCF performance, three kinds of steel piers were designed in this paper, which are shown in Table 6. In this table, W is the width of the web, P/P_y is the axial compression ratio, a is the spacing of transverse partitions, γ/γ^* is the relative stiffness of longitudinal stiffeners; t_s and b_s are the thickness and width of vertical stiffener respectively.

4.3 FE Models of Steel Piers

The experimental study on steel piers carried out by Ge et al. (2013) showed that cracks mostly originated from welded joints at the bottom of piers under horizontal cyclic loads. In order to obtain the equivalent plastic strain history at the crack initiation site and reduce the calculation cost, a hybrid FE model with three element types was established, as shown in Fig. 9. The calculation was carried out using commercial finite element software ABAQUS 6.14. In FE models, horizontal cyclic imposed deformation δ and axial force P are applied on the top of piers to simulate seismic loads and the vertical loads transmitted from the superstructure respectively. Shell element S4R was applied in the range of seismic damage zone length L_d (Zhuge et al. 2019) counted from the bottom of piers; the upper part was simulated by fiber beam element B31; solid element C3D8R was used at the corner of bottom flange and web. The damage length L_d is determined by the following formula:

$$L_d = (2.66\alpha - 0.1) \cdot B \tag{12}$$

where $\alpha = a/B$. For the welded joints simulated by fine solid element, the fillet size h_f was assumed as 6 mm. The minimum mesh size around refined weld toe position was set to 0.2 mm, which is consistent with the characteristic length of Q345qC steel (Liao 2018). The MPC-Beam connection was used between beam elements and shell elements, and the shell-to-solid coupling between shell elements and solid elements was adopted. The bottom of piers was fixed and the whole structure was performed like the form of a cantilever beam. Two kinds of materials were applied according to the actual welding process: for weld foot part, weld material was used; and the other parts were made of Q345qC

Table 6 Steel pier specimens

No.	h (mm)	B (mm)	W/B	λ_B	R_R	P/P_y	a (mm)	γ/γ^*	t (mm)	t_s (mm)	b_s (mm)
S20-30P15	2500	825	1.0	0.20	0.30	0.15	412.5	1.00	20	10	81
S20-40P15	2500	825	1.0	0.20	0.40	0.15	412.5	1.00	15	10	61
S30-30P15	3750	825	1.0	0.30	0.30	0.15	412.5	1.00	20	10	81

For the number (No.) of specimens displayed in the table above, S denotes steel pier structure; the followed three number are slenderness ratio, width-thickness ratio and axial pressure ratio respectively. For example, specimen S20-30P15 represents a steel pier with slenderness of 0.20, width-thickness ratio of 0.30 and axial pressure ratio of 0.15

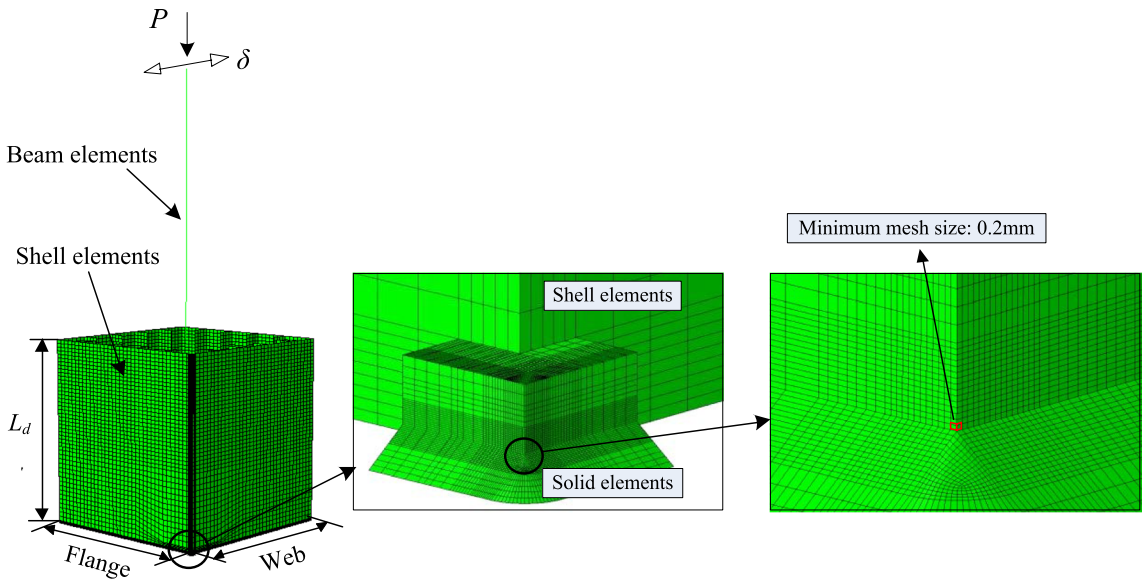

Fig. 9 The FE model for steel piers

base material. Lemaitre–Chaboche hybrid hardening model (Lemaitre and Chaboche 1990) was adopted for the hysteresis constitutive relationship of each material, and its parameters are listed in Table 7, which can be referred from the test conclusions of Liao (2018).

Given that Q345qC steel was used for both notched round bars and steel piers, the CVGM numerical simulation of round bar samples described in Sect. 3 was also carried out according to material constitutive data listed in Table 7; the results N_{hfC} and δ_{C} are shown in Table 4. From the comparison displayed in Table 4, it can be found that N_{hfe}, N_{hfp} and N_{hfC} are more consistent, indicating that CVGM can precisely predict ULCF life with accurately calibrated material parameters.

4.4 Loading Procedure and Life Curves of Steel Piers

Seismic loads in practical projects are simulated by the horizontal imposed deformation applied on the top of piers in FE models, which is expressed in the unit of yield displacement δ_{y}. According to the suggest of Ge et al. (2000), yield displacement δ_{y} of stiffened steel piers with rectangular section consists of bending yield displacement δ_{y1} and shear yield displacement δ_{y2}, which can be expressed as the following form:

$$\delta_{\mathrm{y}} = \delta_{\mathrm{y1}} + \delta_{\mathrm{y2}} = \frac{H_{\mathrm{y}} h^3}{3EI} + \frac{H_{\mathrm{y}} h}{\kappa G A_{\mathrm{s}}} \tag{13}$$

$$\begin{aligned} H_{\mathrm{y}} &= \frac{M_{\mathrm{y}}}{h}\left(1 - \frac{P}{P_{\mathrm{y}}}\right) \\ H_{\mathrm{y}} &= \frac{M_{\mathrm{y}}}{0.85h}\left(1 - \frac{P}{P_{\mathrm{E}}}\right)\left(1 - \frac{P}{P_{\mathrm{u}}}\right) \end{aligned} \tag{14}$$

where I is the moment of inertia; κ is the shear unevenness coefficient of cross section, which is taken as 5/6 herein; G is the shear modulus; A_{s} is the sectional aera; H_{y} is the yield lateral load, which is taken as the smaller value of Eq. (14); M_{y} is the yield bending moment of piers; P is the magnitude of axial load; P_{E} is the Euler's buckling load of a cantilever column; P_{u} is the ultimate strength of steel piers and P_{y} is the yield axial force.

As same as notched round bar validation tests, the numerical simulation of steel piers were also divided into two groups: fitting group and verification group. The fitting tests consist of four different types of CA loading for each kind of steel piers, and the corresponding deformation amplitudes δ are shown in Table 8. While C1 loading, C3 loading and random loading were the loading patterns of verification group. The concepts of CA, C1 and C3 loading are the same as talked in Sect. 3.2 except that the loading is no longer limited in one side. In

Table 7 Chaboche constitutive parameters of Q345qC base metal and weld material (Liao 2018)

Material	$\sigma\vert_0$ (MPa)	Q_∞ (MPa)	b	C_1 (MPa)	γ_1	C_2 (MPa)	γ_2	C_3 (MPa)	γ_3
Base material	354.10	13.2	0.6	44,373.7	523.8	9346.6	120.2	946.1	18.7
Weld material	428.45	17.4	0.4	12,752.3	160.0	1111.2	160.0	630.5	26.0

Table 8 Fitting group data of steel piers

No.	Test 1		Test 2		Test 3		Test 4	
	δ	N_{hf}	δ	N_{hf}	δ	N_{hf}	δ	N_{hf}
S20-30P15	$2.00\delta_{y1}$	49	$2.50\delta_{y1}$	23	$3.00\delta_{y1}$	15	$4.00\delta_{y1}$	7
S20-40P15	$1.50\delta_{y2}$	75	$2.00\delta_{y2}$	27	$2.50\delta_{y2}$	13	$3.00\delta_{y2}$	7
S30-30P15	$2.00\delta_{y3}$	49	$2.25\delta_{y3}$	35	$2.50\delta_{y3}$	25	$3.00\delta_{y3}$	15

δ_{yI}, δ_{yII} and δ_{yIII} represent the yield displacement of S20-30P15, S20-40P15 and S30-30P15 respectively

this section the loading displacement amplitude is half of the corresponding loading displacement range in each half cycle. And the random loading patterns are shown in Fig. 10. Taking the steel pier No. S20-40P15 under C1 loading as an example, the deformation nephogram of the whole structure and the equivalent plastic strain nephogram of the solid part at the critical step are shown in Fig. 11. It can be observed that the equivalent plastic strain accumulates at the corner, which is the vulnerable site in common practice.

The ULCF life of steel piers grouped in fitting was predicted using CVGM, which is shown in Table 8. For each kind of steel piers, four data (δ, N_{hf}) are available. The yield displacements between different kinds of steel pier structures are quite different. Thus, to avoid the excessive volatility of calibrated parameters, a dimensionless form of loading displacement range $2(\delta/\delta_y)$ was adopted to replace $\Delta\delta$ as a reference variable of damage index D. Then the life curve changes to the following form:

$$N_{hf} = A\left[2\left(\delta/\delta_y\right)\right]^C \tag{15}$$

where A and C are constants. Figure 12 shows the life curves of these three steel pier structures.

4.5 Prediction and Comparison

According to life curves obtained in Sect. 4.4 and the loading history of verification group, the corresponding ULCF

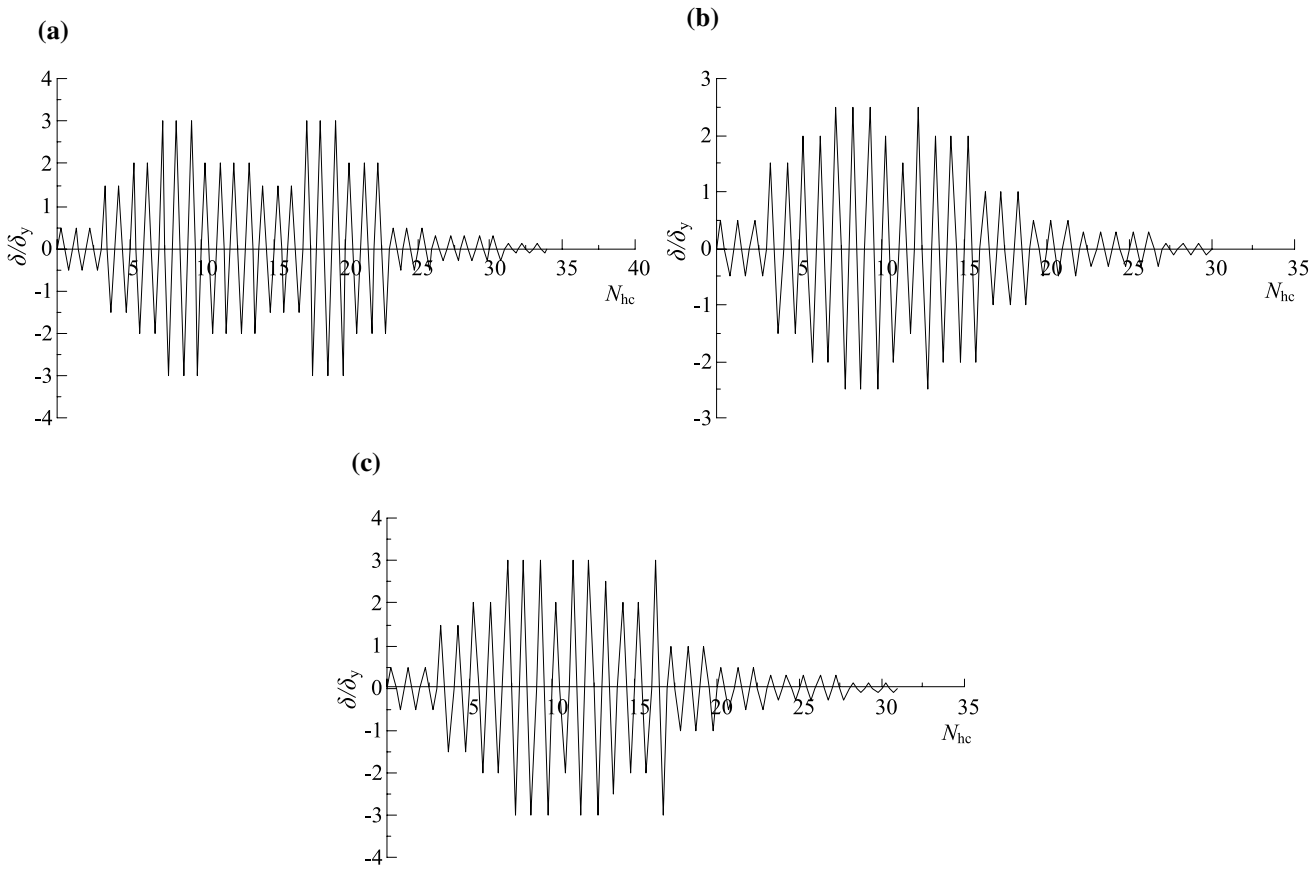

Fig. 10 Random loading patterns of steel piers **a** S20-30P15, **b** S20-40P15 and **c** S30-30P15

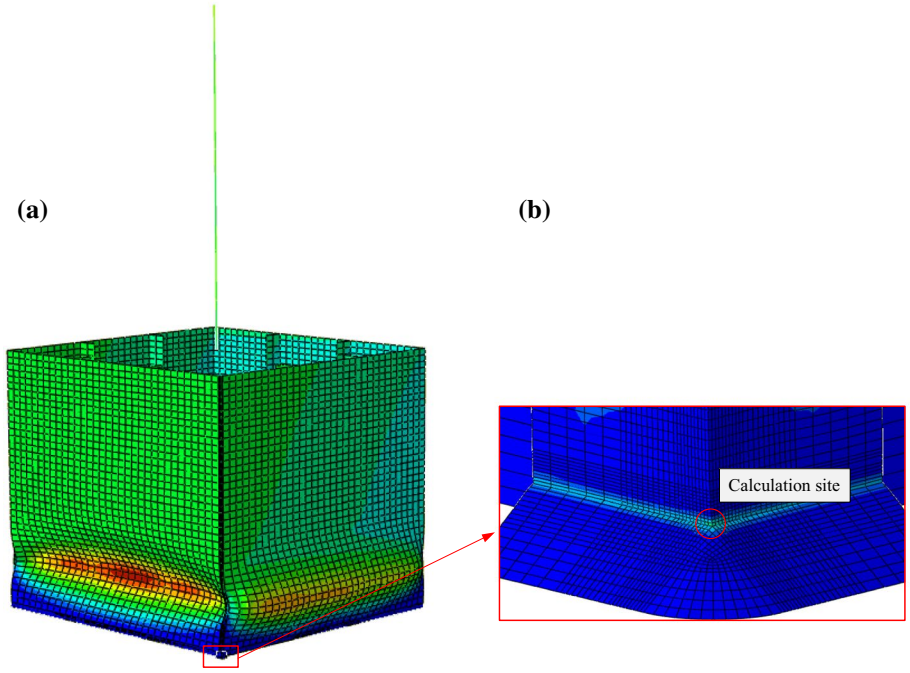

Fig. 11 FE simulation of steel pier No. S20-40P15 under C1 loading **a** deformation nephogram, **b** equivalent plastic strain nephogram

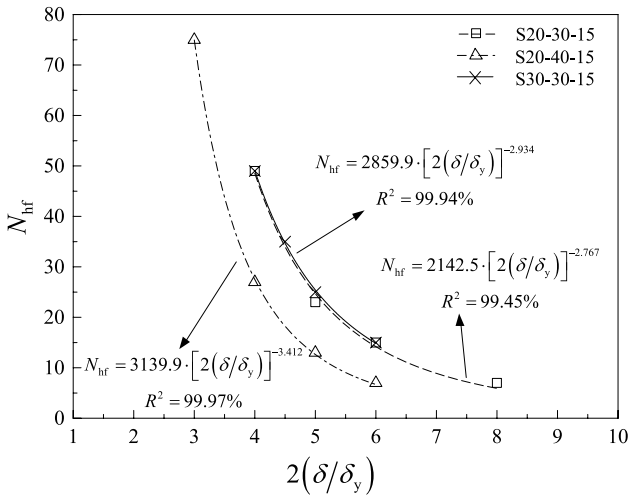

Fig. 12 Life curves of steel piers

life was calculated by the same methods as mentioned in Sect. 3. Table 9 shows the comparison between ULCF life predicted by damage index D and that calculated by CVGM. In order to make a more intuitive comparison, these data were plotted in a coordinate system with abscissa of N_{hfp} and ordinate of N_{hfC} (Fig. 13). It can be observed that all the points are within 20% margin lines. Thus, it can be concluded that ULCF life of steel piers predicted by damage index D is reasonable and convincing.

5 Conclusion and Discussion

Employing the plastic strain amplitude of local regions, traditional methods of evaluating ULCF life are not only computationally intensive but also sensitive to mesh size, which is difficult to apply in practical engineering. To overcome these shortcomings, a new damage index D that combines deformation range $\Delta\delta$, instead of plastic strain range $\Delta\varepsilon$, with the Miner's law was proposed in this paper. According to the life curve of a specific structure, this method could quickly produce an accurate result for the structure ULCF life through its loading mode and proposed damage index D, without complicated numerical simulation. And the influence of triaxial stress state is also considered comprehensively. A total of 24 notched round bar specimens were tested in this paper, of which 14 specimens were used for

Table 9 Verification group data of steel piers

No.	C1 loading		C3 loading		Random loading	
	N_{hfp}	N_{hfC}	N_{hfp}	N_{hfC}	N_{hfp}	N_{hfC}
S20-30P15	10	9	22	21	38	35
S20-40P15	8	9	18	17	29	29
S30-30P15	10	11	23	21	33	33

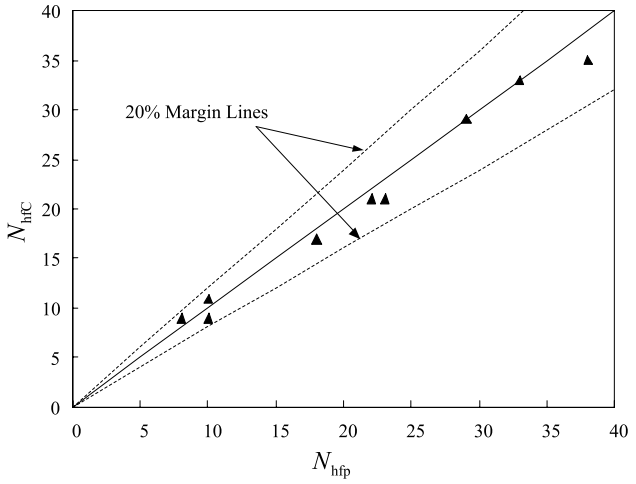

Fig. 13 The comparison between N_{hfC} and N_{hfp}

life curve fitting, and the rest were used for accuracy verification. The comparisons made on the results of 10 notched round bar tests indicated that ULCF life obtained by proposed index D is in a good agreement (within 20% error) with that of experimental tests. The single-column steel piers numerical simulation was also carried out to further verified the effectiveness of the proposed method, showing an acceptable error of 20%. Thus, conclusion can be drawn that the proposed index D can be potentially applied in evaluating the ULCF damage performance of steel structures.

Damage index D is related with life curve, which is the result of experimental analysis and numerical simulation and has a lot to do with the structural form. The main objective of this study is to provide a simple and feasible method for ULCF damage evaluation of steel structures. As for the establishment of a uniform life curve between different steel structural members, future study is required.

Acknowledgements The study described in this paper was supported by the grant from the Natural Science Foundation of China (51878606). Besides, further appreciation is given to Dassault Systèmes Simulia Corporation for the FE simulation of the powerful commercial FE software ABAQUS 6.14.

References

Anderson, T. L. (2005). *Fracture mechanics: Fundamentals and applications* (3rd ed.). Boca Raton: CRC Press.

Bonora, N. (1997). On the effect of triaxial state of stress on ductility using nonlinear CDM model. *International Journal of Fracture, 88*(4), 359–371.

Chen, T., & Tateishi, K. (2007). Extremely low cycle fatigue assessment of thick walled steel pier using local strain approach. *Journal of Structural Engineering, 53A,* 485–492.

Coffin, L. F., Jr. (1954). A study of the effects of cyclic thermal stresses on a ductile metal. *Trans ASME, 76,* 931–950.

Gates, W. E., & Morden, M. (1996). Professional structural engineering experience related to welded steel moment frames following the northridge earthquake. *Structural Design of Tall and Special Buildings, 5*(1), 29–44.

Ge, H. B., Gao, S. B., & Usami, T. (2000). Stiffened steel box columns. Part 1: Cyclic behaviour. *Earthquake Engineering and Structural Dynamics, 29*(11), 1691–1706.

Ge, H. B., & Kang, L. (2012). A damage index-based evaluation method for predicting the ductile crack initiation in steel structures. *Journal of Earthquake Engineering, 16*(5), 623–643.

Ge, H. B., Kang, L., & Tsumura, Y. (2013). Extremely low-cycle fatigue tests of thick-walled steel bridge piers. *Journal of Bridge Engineering, ASCE, 18*(9), 858–870.

Ge, H., & Luo, X. (2011). A seismic performance evaluation method for steel structures against local buckling and extra-low cycle fatigue. *Journal of Earthquake and Tsunami, 05*(02), 83–99.

Ge, H., Ohashi, M., & Tajima, R. (2007). Experimental study on ductile crack initiation and its propagation in steel bridge piers of thick-walled box sections. *Journal of Structural Engineering, JSCE, 53A,* 493–502.

General Administration of Quality Supervision, Inspection and Quarantine of the P.R.C, Standardization Administration of the P.R.C. GB/T 15248-2008, The test method for axial loading constant-amplitude low-cycle fatigue of metallic materials. Beijing: Standard Press of China, 2008.

Hanji, T., Saiprasertkit, K., & Miki, C. (2011). Low-and high-cycle fatigue behaviour of load-carrying cruciform joints with incomplete penetration and strength under-match. *International Journal of Steel Structures, 11*(4), 409–425.

Kang, L., & Ge, H. (2013). Predicting ductile crack initiation of steel bridge structures due to extremely low-cycle fatigue using local and non-local models. *Journal of Earthquake Engineering, 17*(3), 323–349.

Kanvinde, A. M. (2004). Micromechanical simulation of earthquake induced fracture in steel structures.

Kanvinde, A. M., & Deierlein, G. G. (2007). Cyclic void growth model to assess ductile fracture initiation in structural steels due to ultra-low cycle fatigue. *Journal of Engineering Mechanics, 133*(6), 701–712.

Kuwamura, H. (1997). Transition between fatigue and ductile fracture in steel. *Journal of Structural Engineering, 123*(7), 864–870.

Lemaitre, J., & Chaboche, J. L. (1990). *Mechanics of solid materials*. Cambridge: Cambridge University Press.

Li, S. L., Xie, X., & Liao, Y. H. (2019). Improvement of cyclic void growth model for ultra-low cycle fatigue prediction of steel bridge piers. *Materials, 12,* 1615.

Liao, Y. H. (2018). Research on ultra low cycle fatigue properties and fracture mechanism of steel bridge welded joint. Master's thesis, Zhejiang University, Hangzhou, China, 2018 **(in Chinese)**.

Liu, Z., Correia, J., Carvalho, H., et al. (2019). Global-local fatigue assessment of an ancient riveted metallic bridge based on submodelling of the critical detail. *Fatigue and Fracture of Engineering Materials and Structures, 42*(2), 546–560.

Liu, Y., Jia, L. J., Ge, H., et al. (2017). Ductile-fatigue transition fracture mode of welded T-joints under quasi-static cyclic large plastic strain loading. *Engineering Fracture Mechanics, 176,* 38–60.

Manson, S. S. (1965). Fatigue: a complex subject—some simple approximations. *Experimental Mesh, 5,* 193–226.

Nakashima, M., Inoue, K., & Tada, M. (1998). Classification of damage to steel buildings observed in the 1995 Hyogoken-Nanbu Earthquake. *Engineering Structures, 20*(4–6), 271–281.

Okashiro, S., Adachi, Y., et al. (2002). Experimental study on low-cycle fatigue of column base of steel bridge pier under seismic loads. *Journal of Structural Engineering, JSCE, 48A,* 649–655.

Tateish, K., Hanji, T., & Minami, K. (2007). A prediction model for extremely low cycle fatigue strength of structural steel. *International Journal of Fatigue, 29*(5), 887–896.

Tateishi, K., Chen, T., & Hanji, T. (2008). Extremely low cycle fatigue assessment method for un-stiffened cantilever steel columns. *Doboku Gakkai Ronbunshuu A, 64,* 288–296.

Tong, L. W., Huang, X. W., Zhou, F., et al. (2016). Experimental and numerical investigations on extremely-low-cycle fatigue fracture behavior of steel welded joints. *Journal of Constructional Steel Research, 119*(1), 98–112.

Wang, Y. Q., Zhou, H., Shi, Y. J., et al. (2010). Fracture behavior analyses of welded beam-to-column connection based on elastic and inelastic fracture mechanics. *International Journal of Steel Structures, 10*(3), 253–265.

Xie, X., Zhuge, H., Tang, Z., Wang, T., & Liao, Y. (2018). Damage characteristics of thin-walled steel arch bridges subjected to in-plane earthquake action. *Journal of Constructional Steel Research, 151,* 70–82.

Xue, L. (2008). A unified expression for low cycle fatigue and extremely low cycle fatigue and its implication for monotonic loading. *International Journal of Fatigue, 30*(10–11), 1691–1698.

Jia, L. J., Ge, H. B., Suzuki, T., et al. (2015). Experimental study on cracking of thick-walled welded beam-column connections with incomplete penetration in steel bridge piers. *Journal of Bridge Engineering, 20*(4), 1–13.

Zhou, H., Wang, Y. Q., Shi, Y. J., et al. (2013). Extremely low cycle fatigue prediction of steel beam-to-column connection by using a micro-mechanics based fracture model. *International Journal of Fatigue, 48*(2), 90–100.

Zhuge, H., Xie, X., & Tang, Z. (2019). Lengths of damaged zones of steel piers under bidirectional horizontal earthquake components. *China Journal of Highway and Transport, 32*(8), 79–91.